Available online at www.sciencedirect.com
ScienceDirect
Ceramics International 37 (2011) 2561–2567
CERAMICS INTERNATIONAL
www.elsevier.com/locate/ceramint

Structure and properties of plasma sprayed $BaTiO_3$ coatings: Spray parameters versus structure and photocatalytic activity

Pavel Ctibor [a,*], Helene Ageorges [b], Vaclav Stengl [c], Nataliya Murafa [c], Igor Pis [d], Tatiana Zahoranova [d], Vaclav Nehasil [d], Zdenek Pala [a]

[a] *Institute of Plasma Physics, ASCR, Za Slovankou 3, 182 00 Praha 8, Czech Republic*
[b] *CNRS – Laboratoire Sciences des Procedes Ceramiques et de Traitements de Surface (SPCTS), Universite de Limoges, 123 av. A. Thomas, 87060 Limoges Cedex, France*
[c] *Institute of Inorganic Chemistry, ASCR, Husinec-Rez 250 68, Czech Republic*
[d] *Department of Surface and Plasma Science, Faculty of Mathematics and Physics, Charles University, V Holesovickach 2, 180 00 Praha 8, Czech Republic*

Received 31 January 2011; received in revised form 31 March 2011; accepted 1 April 2011
Available online 8 April 2011

Abstract

Plasma spraying enables the creation of layers with thickness in a millimeter range adhering on various substrates. This paper provides a study of phase composition, optical properties and photocatalytic activity of $BaTiO_3$ coatings prepared by atmospheric plasma spraying. The spraying was carried out by a direct current gas-stabilized plasma gun. $BaTiO_3$ was fed into the plasma jet as a feedstock powder prepared by a reactive sintering of micrometer-sized powders of $BaCO_3$ and TiO_2. Microstructure and phase composition are reported and discussed in connection with optical properties and photocatalytic activity. The spraying was carried out by a direct current gas-stabilized plasma gun which normally utilizes spray distance (SD) in frames from 100 to 150 mm. Besides conventional SD 100 mm also extremely high SD 190 mm was used. The color of the sprayed coating is different for each SD and also differs from sintered $BaTiO_3$. X-ray diffraction and also SAD mode of HR-TEM show certain content of amorphous fraction in the coating. The hydrogen content in the coating was found to be higher in the coatings than in the sintered bulk. The diffuse reflectance was measured by UV–VIS spectrophotometry and corresponding band-gap energy was estimated. X-ray photoelectron spectroscopy confirms specific stoichiometric and structural disorder observed also at bang-gap evaluation and by Raman spectroscopy. HR-TEM images for crystalline and amorphous zones are given. Photocatalytic decomposition of acetone was tested and $BaTiO_3$ coatings compared with a sintered bulk.

Keywords: B. Spectroscopy; C. Optical properties; $BaTiO_3$; Plasma spraying; Photocatalysis

1. Introduction

Our recent paper [1] was devoted to mechanical properties and dielectric response of plasma sprayed $BaTiO_3$ at room temperature and around ferroelectric transformation temperature. Now we would like to focus our study on optical response and photocatalytic activity of this specific material.

Barium titanate, $BaTiO_3$, is a multifunctional oxide that exhibits complex phase appearance. Between 120 °C (393 K) and 1457 °C (1730 K) $BaTiO_3$ has a cubic perovskite structure that consists of corner linked oxygen octahedra containing Ti^{4+}, with Ba^{2+}. The melting point is at 1650 °C. [2]. Plasma spraying of $BaTiO_3$ leads typically to mixed crystalline–amorphous structure [3,4]. The interplay between crystalline lattice order and amorphous appearance at the local level has dramatic influence on the behavior of the entire volume of material. A non-uniform band gap structure with a tail of localized states between the nominal values of valence band energy level and conduction band one was shown by the absorbance measurements [5]. A doubly ionized oxygen vacancy with the two extra electrons being donated to the conduction band is described as a factor associated with this behavior [5]. An electron transfer occurring between barium and titanium ions together with the presence of amorphous

* Corresponding author. Tel.: +420 266053717; fax: +420 286586389.
E-mail address: ctibor@ipp.cas.cz (P. Ctibor).

0272-8842/$36.00
doi:10.1016/j.ceramint.2011.04.003

clusters may introduce delocalized electronic levels in the forbidden gap [5].

In crystalline $BaTiO_3$ the bonding between Ba and TiO_6 is ionic, while a covalent bonding nature exists between Ti and O as results of the hybridization between the O(2p) and Ti(3d) states [6]. In structurally disordered $BaTiO_3$ a weak contribution of Ba states to the density of states of the valence band (dominated by oxygen contribution) and a significant contribution of the Ba and Ti for the conduction band states are taking place [5]. The specific character of the absorption edge with a tail on the Tauc plot has been previously identified for a large number of semiconductors and can originate from number of mechanisms including (i) the presence of point defects; (ii) extended states at the valence or conduction bands; (iii) disordered structure or the presence of inhomogeneous strain in the semiconductor, e.g. as for GaN [7]. The photochemical activity of the states from this tail is claimed to be high enough to reduce O_2 to the superoxide anion, leading e.g. to peroxidation of lipids in a photocatalytic application [8]. Structurally ordered, crystalline, ferroelectric $BaTiO_3$ is not expected to exhibit such features but plasma sprayed $BaTiO_3$ with amorphous fraction and possible presence of color centers is a candidate for it.

X-ray photoelectron spectroscopy (XPS) is a surface analytical technique providing information on the chemical states of the constituents and their atomic concentrations. Since $BaTiO_3$ is a wide band gap material, it exhibits electrostatic charging during the XPS measurements [9]. This problem can be however diminished by relating the photoelectron binding energies to the C 1s peak. Presence of hydrogen in $BaTiO_3$ film is connected with formation of OH groups [10] or presence of protons [11], as mentioned also in our previous paper [1].

$BaTiO_3$ was demonstrated to promote photocatalytic decomposition of diclofop methyl [12], Safranin T [13], or methylene blue [14]. Adsorption of gaseous acetone on brookite, anatase, and rutile TiO_2 nanoparticles shows typical infrared absorption bands at 1242, 1370, 1424, and 1690 cm^{-1}, albeit slightly shifted compared with liquid-phase acetone [15]. In our present paper we are studying the kinetics of gaseous acetone decomposition as well as the kinetics of its end-products (CO_2 and CO) growth.

2. Experimental

Feedstock powder and substrate material as well as the plasma spraying process are described precisely elsewhere [1]. $BaTiO_3$ feedstock powder was obtained by crushing and sieving of sintered coarse agglomerates. Barium titanate was sprayed at arc power 30 kW with a gas-stabilized plasma (GSP) gun and atmospheric plasma spraying (APS) process. The spray distance (SD) was 100 and 190 mm for the short SD and long SD coatings, respectively. The plasma spraying deposition time was about 5 min to reach a thickness of 0.9–1.0 mm in the case of short SD. For the long-SD coatings, where the spray efficiency is markedly lower, the same spraying cycle led to a thickness of typically only 0.3–0.4 mm.

For microscopic observation, polished cross sections of coatings were prepared. The microstructure of plasma deposits was studied by optical microscopy. The bulk density of powders was measured by pycnometry. X-ray diffraction (XRD) was performed as a phase identification with SIEMENS D500™ equipment which allowed identifying present phases within powder and coatings. For estimation of the crystallinity of the plasma sprayed coatings relative peak areas have been used. These have been calculated from relative ratios of the areas of the three main peaks (1 0 1, 1 1 1 and 2 0 0) from the tetragonal barium titanate phase.

The content of hydrogen was measured by the LECO technique (Leco RH 404 apparatus). This technique is based on melting of a small amount of a material whereas the spectral analysis of the melt provides a quantitative evaluation of the content of low-concentration admixtures. The quantity of material analyzed was 1 g for each sample.

Lattice spacing and the phase of $BaTiO_3$ coatings were analyzed by High Resolution Transmission Electron Microscope (HR-TEM) Jeol JEM 3010 and Selected Area Electron Diffraction (SAED).

The diffuse reflectance was measured by UV–VIS–NIR scanning spectrophotometer (Shimadzu, Japan) with a multipurpose large sample compartment and the corresponding band-gap energy was estimated. The reflectance curves, obtained between 200 and 2000 nm were then converted to absorbance and recalculated [16] to bandgap energy E_{bg}.

Raman spectroscopy was performed using a Lambda Solutions P1 apparatus – laser wavelength 785 nm, objective 50×, integration time 25 s. The surface of the coating was polished before the test.

The X-ray photoelectron spectroscopy (XPS) was measured on coatings and compared with feedstock powder. Experiments were carried out in an ultra-high vacuum chamber with a base pressure lower than 5×10^{-7} Pa. XPS experiments were performed using an Omicron EA 125 multichannel hemispherical analyzer with Al K-alpha line (1486.6 eV) as a primary photon source. To exclude charging effects during the XPS experiments, photoelectron binding energies (EB) were referenced to the C 1s peak, which was assumed to be positioned at a constant binding energy EB = 284.6 eV.

Photocatalytic decomposition of acetone was tested and $BaTiO_3$ coatings compared with a sintered bulk (sintering in a laboratory furnace in an air atmosphere, heating rate 7 °C/min, dwell time 120 min at 1300 °C, cooling rate 7 °C/min). Kinetics of the photocatalytic degradation of gaseous acetone was measured by using a self-constructed stainless steel photoreactor (see Fig. 1) with fluorescent lamp Narva LT8WT8/073BLB, a black lamp with 365 nm wavelength and input power 8 W (light intensity 6.3 mW/cm^2). The gas concentration was measured with the use of quadrupole mass spectrometer JEOL JMS-Q100GC and gas chromatograph Agilent 6890N. A high resolution gas chromatography column (19091P-QO4, J&W Scientific) was used. The sample from the reactor was taken via a sampling valve at time intervals of 2 h for CO_2 and CO, whereas for acetone the intervals were shorter and not exactly the same for all samples. The total volume of the reactor was 3.5 l, filled with oxygen, at a flow rate of 1 l/min.

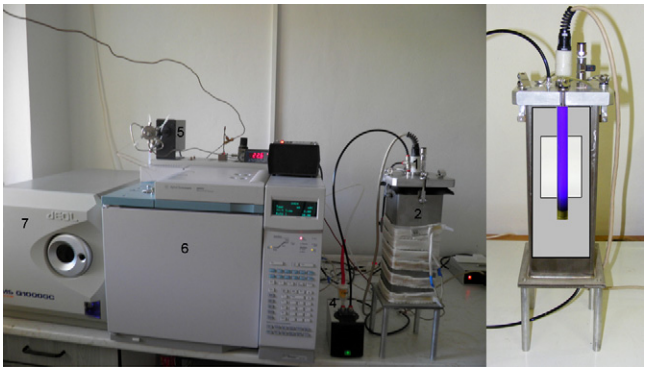

Fig. 1. Set-up for the photocatalytic test: 1 – UV lamp; 2 – stainless steel reaction chamber; 3 – tested sample placed inside (depicted as a white rectangle on the right schematic view); 4 – membrane pump; 5 – sampling valve; 6 – gas chromatograph; 7 – mass spectrometer.

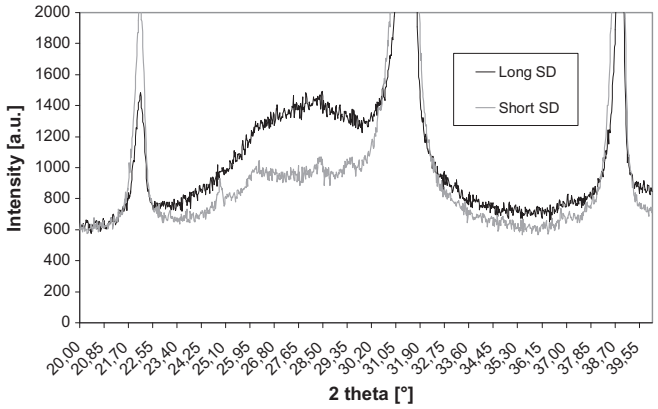

Fig. 2. XRD pattern detail – comparison of long SD and short SD coatings.

3. Results and discussion

The micrographs of cross sections and in-plane sections of the coatings were published earlier [1]. The XRD pattern, Fig. 2, corresponds strictly to the tetragonal phase (PDF2 Card No. 01-081-2204), which was confirmed to be the constituent of the feedstock powder as well as of the coatings. The intensity ratio of individual peaks of the feedstock as well as of the coatings is very similar to patterns reported in the literature [17]. In the coating, a certain quantity of amorphous phase is present, which manifested itself by a halo centered around 28° 2θ in the pattern, and quantified as 30% for long SD and 10% for short SD. The dark color of the short SD coating surface indicates oxygen deficiency, see Fig. 3. The bulk density of the short SD coating as measured by pycnometry is 5365 ± 2 kg m^{-3}, whereas the bulk density of the long SD coating measured by the same technique is only 4940 ± 3 kg m^{-3}.

High Resolution Transmission Electron Microscope (HR-TEM) showed the presence of crystalline zones and amorphous zones in the short-SD coating (see Fig. 4). The sample exhibits amorphous zones represented by zone A with SAD pattern on the left and crystalline zones with tetragonal structure of $BaTiO_3$ and interlayer spacing 0.281 nm corresponding to [1 1 0] direction (see zone B with SAD pattern on the right). In the crystalline material, in several places ferroelectric domains were visible, se zone C in Fig. 4.

Fig. 3. Comparison of long SD and short SD coatings surfaces – the dark color of the short SD coating (right) indicates oxygen deficiency; sample width is 25 mm.

The short-SD coating has hydrogen content of 46 ppm, whereas long-SD coating exhibits only 18 ppm. The sintered reference sample exhibits at the same test just 6 ppm of hydrogen. These values correspond to the fact that coating with a short SD means melting and solidification in the hydrogen-rich plasma gas atmosphere. The beginning of thermal history is identical in the case of the long SD sample. However,

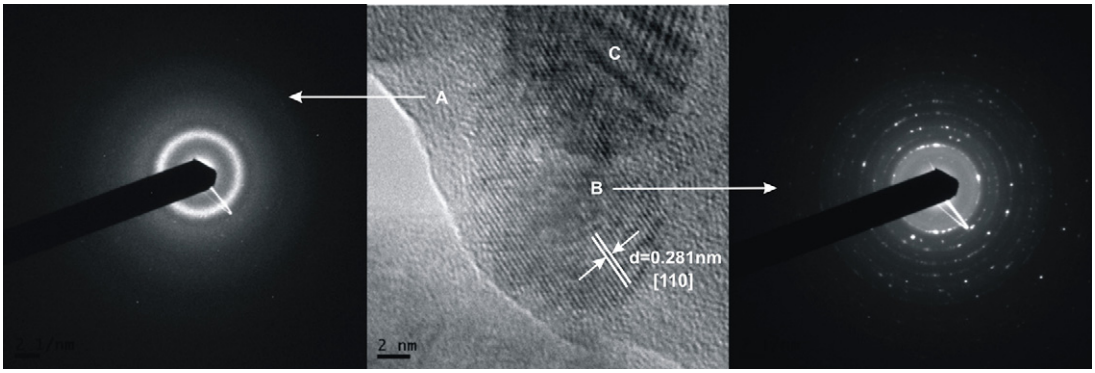

Fig. 4. HR-TEM image – amorphous zone A with SAD pattern on the left, crystalline zone B with SAD pattern on the right and zone C exhibiting ferroelectric domains.

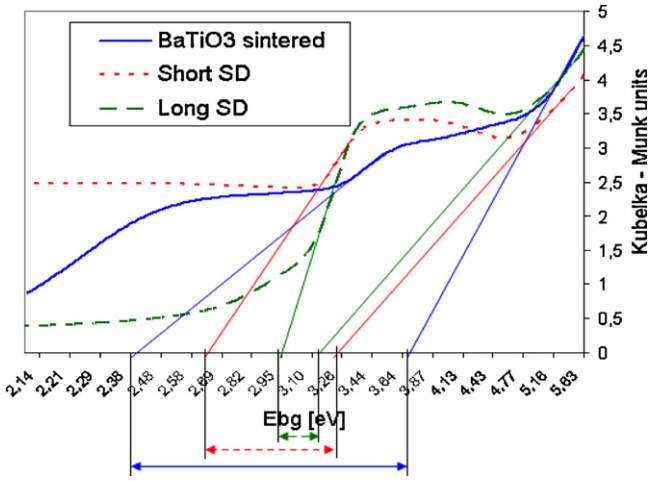

Fig. 5. Bandgap energy estimation.

particles building this sample are during their long flight also surrounded with ambient air that is entrained into the plasma intensively [18]. This air contributes to re-oxidation. The sintered sample was heated in the furnace in air atmosphere, but its heating was not only carried out at much lower temperature and also in a nearly hydrogen-free environment. The only hydrogen available could come from the moisture present always in air.

A bandgap estimation [19,20] of the coatings in comparison with a sintered sample is given in Fig. 5. The bandgap estimation was done assuming indirect transition, because of expected presence of the donor levels [11] within the bandgap, introduced into the structure by hydrogen atoms. Both coatings exhibit red shift compared to the sintered sample. This shift is more markedly pronounced for the long SD coating. The bandgap value reported for thin films range from 3.72 eV to 3.92 eV [21] depending on powder and processing details. The dark blue color of strongly reduced $BaTiO_3$ (in our case: short SD) is attributed to small-polaron hopping by electrons of Ti^{3+}–Ti^{4+} charge transfer type and gives evidence of the strongly disordered nature of the material [22]. Our sintered $BaTiO_3$ sample exhibits a main absorption edge with bandgap energy E_{bg} at 3.68 eV, which corresponds to crystalline structure [5]. The same sample has also a secondary absorption edge with excitation energy E at 2.40 eV, which seems to be associated with amorphous structure [5]. Moreover, it exhibits also an

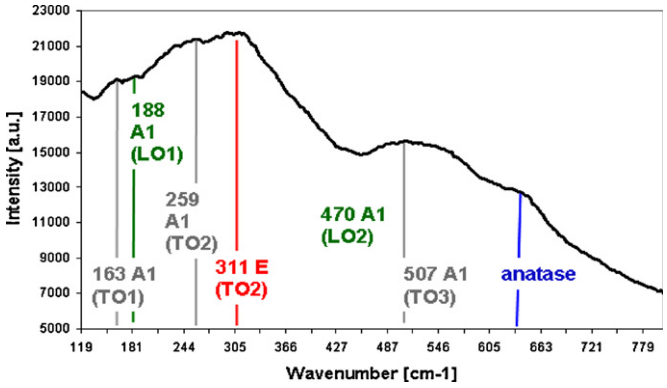

Fig. 6. Raman spectrum of the short SD coating.

absorption tail of delocalized electronic states [5,6,8] with excitation energy $E < 2$ eV.

Similarly, the short-SD $BaTiO_3$ coating exhibits a main absorption edge with bandgap energy E_{bg} at 3.25 eV (crystalline), a secondary absorption edge with excitation energy E at 2.64 eV (amorphous) and a tail of delocalized states.

The long-SD $BaTiO_3$ coating exhibits main absorption edge with bandgap energy E_{bg} at 3.12 eV (crystalline), a secondary absorption edge with excitation energy E at 2.95 eV (amorphous) and a tail of delocalized states.

Because of smaller step between amorphous and crystalline excitation energy of the long-SD coating it is probable that the structural disorder in this sample is of different nature compared to the short-SD coating.

The states forming the tail could be the shallow donor levels induced by H-protons within the bandgap in titanates [11], as mentioned by us [1] in the discussion of dielectric behavior of the plasma sprayed $BaTiO_3$ coatings.

Raman spectrum of the short-SD coating is displayed in Fig. 6. The pattern with peaks at 311 and 507 cm^{-1} corresponds to tetragonal phase of $BaTiO_3$ [23]. At low oxygen pressure, which is the situation relevant for plasma spraying, the density of oxygen vacancies is higher, and the expansion of the lattice volume is greater [23]. This is why the Raman modes shift to lower frequencies: 507 cm^{-1} in our case instead of 518 cm^{-1} [6] or 532 cm^{-1} in [23] for the A_1 torsion mode. The Raman spectrum of the long-SD coating is practically identical.

The modes further split into longitudinal (LO) and transverse (TO) components. The spectrum in Fig. 6 shows

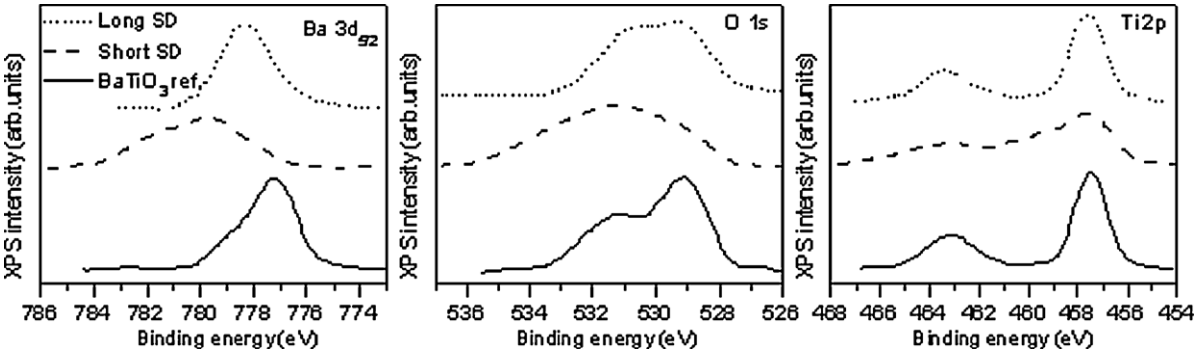

Fig. 7. XPS spectra of the $BaTiO_3$ feedstock powder, short SD and long SD coatings.

the stretching mode of A1(TO_1), A1(TO_2) and A1(TO_3) at around 163, 259 and 507 cm^{-1}, respectively [6,15]. The stretching mode of E (TO_2) appeared at 311 cm^{-1}, while A1(LO_1) stretching modes appeared at 188 cm^{-1} and A1(LO_2) at about 470 cm^{-1} [6]. However, the last one was not very pronounced in our case. By the Raman spectroscopy, presence of TiO_2 in anatase form was detected in our sample, as mentioned in the literature [24,25]. One of the Raman-active fundamental modes – the peak at about 645 cm^{-1} was observed in TiO_2 film [24] or coating [25]. Elsewhere [26] such a peak was shown without comments. In our case also a weak peak at 631 cm^{-1} was detected, which can correspond to individual anatase-TiO_2 phase in the $BaTiO_3$ coating.

X-ray photoelectron spectroscopy revealed certain mismatch in the stoichiometry and also different chemical composition of the surfaces for the different coatings. Fig. 7 displays Ba $3d_{5/2}$, O 1s and Ti 2p photoemission spectra of the coatings as well as the reference feedstock powder. The binding energy of Ti $2p_{3/2}$ peak (457.4 eV) is in good agreement with previous XPS studies on $BaTiO_3$ [27,28]. The O 1s spectra revealed several components. The O1s spectrum of the feedstock powder can be deconvoluted into a component at the energy of 529.1 eV, which corresponds to $BaTiO_3$, and a component at 531.2 eV, which was previously identified as belonging to hydroxyl groups typical for adsorbed water [29]. Taking into account merely the low energy component of O 1s, the intensities of the Ba, Ti, and O core level peaks give an element ratio Ba:Ti:O: equal to 1:1:3, in accordance with expected stoichiometric value. On the other hand, the XPS spectra of the long-SD sample give the element ratio equal to 2:3:9, which deviates from the expected value and indicates the decrease of Ba atomic concentration within the XPS sampling depth (ca. 4 nm). The estimation of the concentration ratio for the short-SD is complicated due to the complex O 1s spectrum which contains components also at higher binding energies (above 532 eV) related to other surface contaminants. However, an element ratio Ba:Ti, equal to 1:2, indicates even larger decrease of Ba concentration as it was in the case of the long-SD sample. Ba $3d_{5/2}$ spectra indicate that barium is in a different chemical state in all coating samples compared to the feedstock powder. The powder and long-SD Ba peaks can be decomposed into two components at the binding energies of 777.1 eV (Ba I) and 778.5 eV (Ba II). The Ba 3d state is very sensitive onto all structural and chemical environment changes, as such transition from crystalline to amorphous phase [30], change in the number of neighbor O atoms [31], or formation of BaO. The Ba I component, as the prevailing part of the powder XPS spectrum, can be assigned to polycrystalline $BaTiO_3$, while the presence of the Ba II component is the consequence of defects in crystalline $BaTiO_3$ structure. In the case of the long-SD sample, the BaII component prevails and it can be assigned to amorphous $BaTiO_3$ in accordance with Ref. [27] and XRD measurements that revealed rather high amount of the amorphous phase. The Ba $3d_{5/2}$ spectrum of the short-SD sample deviates from the reference powder even more, which might be the consequence of the surface contamination, as indicated by theO 1s spectrum.

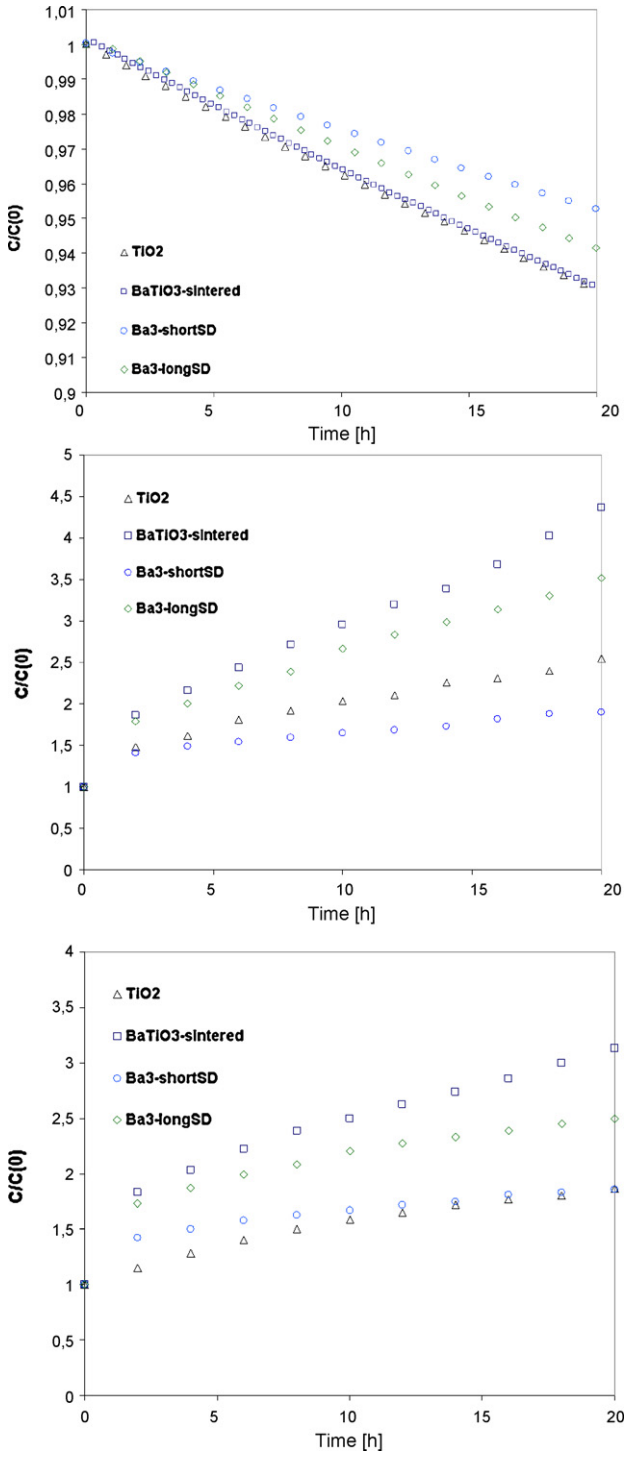

Fig. 8. Acetone decomposition (a) and CO_2 (b) as well as CO (c) increase.

Kinetics of the photocatalytic decomposition of acetone is shown in Fig. 8. C is the actual concentration and C_0 the initial one for each gas. The decrease of acetone concentration was nearly identical for the sintered $BaTiO_3$ as for typical plasma sprayed TiO_2, Fig. 8a, whereas long-SD $BaTiO_3$ coating was less effective and short-SD $BaTiO_3$ coating even less. Fig. 8b brings carbon dioxide increase kinetics. Here the highest quantity was detected for sintered $BaTiO_3$, followed by long-SD $BaTiO_3$ coating, whereas the short-SD $BaTiO_3$ coating was

even less efficient than typical plasma sprayed TiO_2. Exactly the same order of samples we got when observing the carbon monoxide evolution, Fig. 8c. The short-SD $BaTiO_3$ coating is here better than TiO_2 coating at the beginning of the test period but the trend seems to lead to a saturation at about $C/C_0 = 1.8$.

From Fig. 8 we can conclude that for photocatalytic decomposition of gaseous acetone at 365 nm (i.e. 3.40 eV) to its end products, the most efficient surface is sintered $BaTiO_3$, followed by long-SD $BaTiO_3$ coating and further by the short-SD $BaTiO_3$. The first two samples demonstrated in our experiments higher photocatalytic activity than typical plasma sprayed TiO_2 whereas the third sample showed lower activity.

4. Conclusions

The quantity of amorphous fraction seems to correlate with the excitation energy of the secondary absorption edge. Oxygen vacancies are the defects forming the oxygen-deficient nature of the plasma sprayed coatings as opposed to TiO_2, where stacking faults in the lattice were observed [32].

In the sintered sample case a secondary absorption edge associated with structural disorder of Ba and Ti is responsible for the photocatalytic behavior. In the case of both coating types the hydrogen-induced donor levels in the bandgap are the dominant features (also the presence of some anatase TiO_2 on the surface). In the case of long-SD coating the structural disorder associated with high amorphous content decreases the photocatalytic ability. In the case of short-SD coating the Ba loss from the structure during the spraying process seem to be high and affect the photocatalytic efficiency strongly. When we are speaking about ''photocatalytic efficiency'', it is necessary to note that this feature is associated with certain substance (acetone), certain wavelength (365 nm) and other details of the set-up, while for completely different set-up it could differ markedly.

Acknowledgments

This work was supported by the Grant Agency of the Academy of Sciences of the Czech Republic (Project No. IAAX00430803) and by research program MSM 0021620834 financed by the Ministry of Education of the Czech Republic. I. Pis also thanks to the Grant Agency of the Czech Republic (Grant No. 202/09/H041) for the research support.

References

[1] P. Ctibor, H. Ageorges, J. Sedlacek, R. Ctvrtlik, Structure and properties of plasma sprayed $BaTiO_3$ coatings, Ceramics International 36 (2010) 2155–2162.
[2] M.H. Zhao, D.A. Bonnell, J.M. Vohs, Effect of ferroelectric polarization on the adsorption and reaction of ethanol on $BaTiO_3$, Surface Science 602 (2008) 2849–2855.
[3] Y.M. Kim, K.H. Baik, K.S. Park, Microstructure evolution and dielectric properties of plasma sprayed $BaTiO_3$ coatings, in: B.R. Marple, M.M. Hyland, Y.C. Lau, C.J. Li, R.S. Lima, G. Montavon (Eds.), Proceedings of International Thermal Spray Conference, 2009, pp. 547–550.
[4] S. Sampath, Thermal spray applications in electronics and sensors: past, present and future, Journal of Thermal Spray Technology 19 (5) (2010) 921–949.
[5] F.M. Pontes, C.D. Pinheiro, E. Longo, E.R. Leite, S.R. de Lazaro, R. Magnani, P.S. Pizani, T.M. Boschi, T.M. Boschi, F. Lanciotti, Theoretical and experimental study on the photoluminescence in $BaTiO_3$ amorphous thin films prepared by the chemical route, Journal of Luminescence 104 (2003) 175–185.
[6] I.A. Souza, M.F.C. Gurgel, L.P.S. Santos, M.S. Goes, S. Cava, M. Cilense, I.L.V. Rosa, C.O. Paiva-Santos, E. Longo, Theoretical and experimental study of disordered $Ba_{0.4}Sr_{0.55}TiO_3$ photoluminescence at room temperature, Chemical Physics 322 (2006) 343–348.
[7] P.P.-T. Chen, K.S.A. Butcher, E.M. Goldys, T.L. Tansley, K.E. Prince, High energy Urbach characteristic observed for gallium nitride amorphous surface oxide, Thin Solid Films 496 (2006) 342–345.
[8] V. Nadtochenko, N. Denisov, A. Gorenberg, Y. Kozlov, P. Chubukov, J.A. Rengifo, C. Pulgarin, J. Kiwi, Correlations for photocatalytic activity and spectral features of the absorption band edge of TiO_2 modified by thiourea, Applied Catalysis B: Environmental 91 (2009) 460–469.
[9] E.K. Evangelou, N. Konofaos, X. Aslanoglou, S. Kennou, C.B. Thomas, Characterization of $BaTiO_3$ thin films on p-Si, Materials Science in Semiconductor Processing 4 (2001) 305–307.
[10] J. Chimborazo, M. Castillo, C. Velasco, A. Stashans, H atom in $BaTiO_3$ and $CaTiO_3$ crystals: structure, electronic properties, and diffusion, Proceedings of SPIE Advanced Organic and Inorganic Optical Materials 5122 (2003) 280.
[11] F. El Kamel, P. Bonin, Proton related defects in a-$BaTiO_3$:H films based MIM capacitors, Solid State Ionics 180 (2009) 853–856.
[12] L. Gomathi Devi, G. Krishnamurthy, TiO_2/$BaTiO_3$-assisted photocatalytic mineralization of diclofop-methyl on UV-light irradiation in the presence of oxidizing agents, Journal of Hazardous Materials 162 (2009) 899–905.
[13] V. Sydorchuk, S. Khalameida, V. Zazhigalov, Mechanochemical synthesis of barium titanate and its photocatalytic properties, Annales universitatis Mariae Curie-Sklodowska 64 (11) (2009) 159–168.
[14] Y.-H. Chen, Y.-D. Chen, Kinetic study of Cu(II) adsorption on nanosized $BaTiO_3$ and $SrTiO_3$ photocatalysts, Journal of Hazardous Materials 185 (2011) 168–173.
[15] A. Mattsson, L. Oesterlund, Adsorption and photoinduced decomposition of acetone and acetic acid on anatase, brookite, and rutile TiO_2 nanoparticles, Journal of Physical Chemistry 114C (2010) 14121–14132.
[16] M.K. Reddy, S.V. Manorama, A.R. Reddy, Bandgap studies on anatase titanium dioxide, Materials Chemistry and Physics 78 (2002) 239–245.
[17] X. Wang, L. Zhang, H. Liu, J. Zhai, X. Yao, Dielectric nonlinear properties of $BaTiO_3$–$CaTiO_3$–$SrTiO_3$ ceramics near the solubility limit, Materials Chemistry and Physics 112 (2008) 675–678.
[18] J.R. Fincke, D.M. Crawford, S.C. Snyder, W.D. Swank, D.C. Haggard, R.L. Williamson, Entrainment in high-velocity, high-temperature plasma jets Part I: experimental results, International Journal of Heat and Mass Transfer 46 (2003) 4201–4213.
[19] J.C. Colmenares, M.A. Aramendia, A. Marinas, J.M. Marinas, F.J. Urbano, Synthesis, characterization and photocatalytic activity of different metal-doped titania systems, Applied Catalysis A: General 306 (2006) 120–127.
[20] D. Reyes-Coronado, G. Rodriguez-Gattorno, M.E. Espinosa-Pesqueira, C. Cab, R. de Coss, G. Oskam, Phase-pure TiO_2 nanoparticles: anatase, brookite and rutile, Nanotechnology 19 (2008) 145605 (10 pp.).
[21] H.X. Zhang, C.H. Kam, Y. Zhou, X.Q. Han, Y.L. Lam, Y.C. Chan, K. Pita, Optical and electrical properties of sol–gel derived BaTiO3 films on ITO coated glass, Materials Chemistry and Physics 63 (2000) 174–177.
[22] M. Schrader, D. Mienert, T.-S. Oh, H.-I. Yoo, K.D. Becker, An optical, EPR and electrical conductivity study of blue barium titanate, $BaTiO_3$-δ, Solid State Sciences 10 (2008) 768–775.
[23] H.Z. Guo, Z.H. Chen, B.L. Cheby, H.B. Lu, L.F. Liu, Y.L. Zhou, Structure dynamics of strongly reduced epitaxial $BaTiO_{3-x}$ studied by Raman scattering, Journal of the European Ceramic Society 25 (2005) 2347–2352.
[24] C. Giolli, F. Borgioli, A. Credi, A. Di Fabio, A. Fossati, M. Muniz Miranda, S. Parmeggiani, G. Rizzi, A. Scrivani, S. Troglio, A. Tolstoguzov, A. Zoppi, U. Bardi, Characterization of TiO_2 coatings prepared by a modified electric arc-physical vapour deposition system, Surface and Coatings Technology 202 (2007) 13–22.

[25] I. Burlacov, J. Jirkovsky, L. Kavan, R. Ballhorn, R.B. Heimann, Cold gas dynamic spraying (CGDS) of TiO_2 (anatase) powders onto poly(sulfone) substrates: microstructural characterisation and photocatalytic efficiency, Journal of Photochemistry and Photobiology A: Chemistry 187 (2007) 285–292.

[26] T. Ostapchuk, J. Pokorny, A. Pashkin, J. Petzelt, V. Zelezny, D. Rafaja, I. Drbohlav, Soft-mode spectroscopy of $BaTiO_3$ thin films, Journal of the European Ceramic Society 25 (2005) 3063–3067.

[27] D. Ehre, H. Cohen, V. Lyahovitskaya, I. Lubomirsky, X-ray photoelectron spectroscopy of amorphous and quasiamorphous phases of $BaTiO_3$ and $SrTiO_3$, Physics Review B 77 (2008) 184106.

[28] S. Kumar, V.S. Raju, T.R.N. Kutty, Investigations on the chemical states of sintered barium titanate by X-ray photoelectron spectroscopy, Applied Surface Science 206 (2003) 250–261.

[29] B. Chornik, V.A. Fuenzalida, C.R. Grahmann, R. Labbe, Water adsorption properties of amorphous $BaTiO_3$ thin films, Vacuum 48 (1997) 161–164.

[30] D. Ehre, H. Cohen, V. Lyahovitskaya, A. Tagantsev, I. Lubomirsky, Structural transformations during formation of quasi-amorphous $BaTiO_3$, Advanced Functional Materials 17 (2007) 1204–1208.

[31] P.A.W. van der Heide, Surface core level shifts in photo-electron spectra from the Ca, Sr and Ba titanates, Surface Science 490 (2001) L616–626.

[32] L.A. Bursill, B.G. Hyde, Crystallographic shear in the higher titanium oxides: structure, texture, mechanisms and thermodynamics, in: H. Reiss, J.O. McCaldin (Eds.), Progr. Solid State Chem., vol. 7, 1972, p. 177/253.